A PV Micro-inverter With PV Current Decoupling Strategy

Chien-Yao Liao, *Student Member, IEEE*, Wen-Shiun Lin, Yaow-Ming Chen, *Senior Member, IEEE*,
and Cheng-Yen Chou, *Member, IEEE*

***Abstract*—The objective of this paper is to propose a novel photovoltaic (PV) micro-inverter with PV current decoupling (PVCD) strategy to achieve maximum power point tracking (MPPT) performance without using large electrolytic capacitors. Conventionally, the grid-connected PV micro-inverter needs a large PV-side electrolytic capacitor to suppress the double-line frequency voltage ripple, which is caused by the injected ac grid power, to achieve the desired MPPT performance. However, the short lifetime electrolytic capacitor will reduce the PV micro-inverter's reliability dramatically. Therefore, different active power decoupling circuits (APDCs) have been proposed in published papers to reduce the required input capacitance so that the long lifetime film capacitor can be used to replace the electrolytic capacitor. Unlike the conventional APDC with charging and discharging modes operation, a novel PVCD strategy, which is based on the concept of current decoupling instead of power decoupling, is proposed to simplify the control mechanism of the PV micro-inverter. Furthermore, to accomplish the proposed current decoupling concept, a novel circuit topology for the PV micro-inverter is also proposed. With the proposed PVCD strategy, the current decoupling tank (CDT) inside the proposed PV micro-inverter can buffer the current difference between the constant current from the PV panel and the rectified sinusoidal current of the ac grid current. Therefore, the input capacitance on the PV-side can be reduced dramatically and the long lifetime film capacitor can be used to replace the electrolytic capacitor. The reliability of the PV micro-inverter with good MPPT performance can be increased. In this paper, the operation principle and the component design of the proposed PV micro-inverter with PVCD strategy will be presented. Simulation results and experimental results of a prototype 240 W PV micro-inverter is shown to verify the performance of the PV micro-inverter with PVCD strategy.**

***Index Terms*—Active power decoupling circuit (APDC), current decoupling tank (CDT), film capacitor, maximum power point tracking (MPPT), photovoltaic (PV) micro-inverter, PV current decoupling (PVCD).**

I. INTRODUCTION

WITH increasing concern of energy crisis and environmental issues, renewable energy sources, mainly for solar and wind energy, have attracted the attention in academia and industry. Due to the advantages of easy maintenance, long lifetime, and no rotational parts, the installation capacity of photovoltaic (PV) power generation system has been increased continuously [1], [2]. The PV energy has been widely used all over the world and has become an important source of electricity provider for residences and industries.

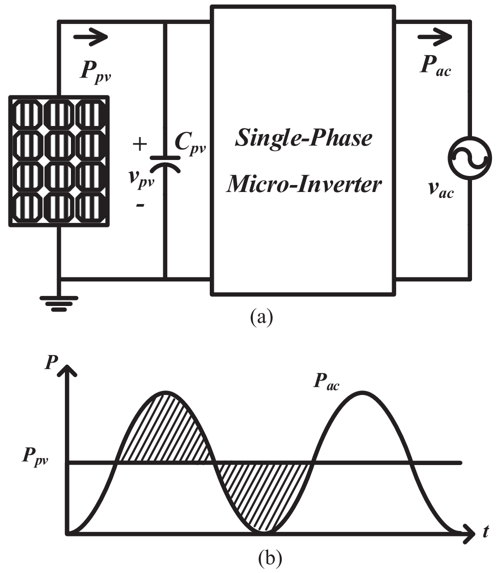

(a)

(b)

Fig. 1. Corresponding power waveforms to PV micro-inverter. (a) Conceptual circuit diagram of single-phase PV micro-inverter. (b) Instantaneous power waveforms.

For the PV power generation system, grid-connected inverters are commonly used to transfer PV power into the power grid. The grid-connected PV inverters are commonly classified as the centralized inverter, the string inverter, and the micro-inverter [3]. Among them, the PV micro-inverter system is well known for mitigating the shading effect and mismatch problem since each PV panel can deliver its own maximum power without affecting others. Moreover, the PV micro-inverter has the advantages of easy "Plug-N-Play," low installation cost, and high flexibility [3]. Many studies on PV micro-inverters are presented for efficiency improvement, cost reduction, and reliability increase [4]–[16].

The conceptual circuit diagram of the PV micro-inverter with its corresponding power waveforms are shown in Fig. 1. The PV micro-inverter will draw the constant maximum power from the PV panel while delivering double-line-frequency power into the

---

Manuscript received December 22, 2015; revised May 6, 2016 and August 1, 2016; accepted September 27, 2016. Date of publication October 11, 2016; date of current version March 24, 2017. Recommended for publication by Associate Editor Robert C. N. Pilawa-Podgurski.

C.-Y. Liao, W.-S. Lin, and Y.-M. Chen are with the Electric Energy Processing Laboratory (EEPro), Department of Electrical Engineering, National Taiwan University, Taipei 10617, Taiwan (e-mail: f98921088@ntu.edu.tw; r00921069@ntu.edu.tw; ymchen@cc.ee.ntu.edu.tw).

C.-Y. Chou is with Darfon Electronic Corp., Taoyuan 333, Taiwan, and also with the National Taiwan University of Science and Technology, Taipei 106, Taiwan (e-mail: lyapunov@mail2000.com.tw).

Color versions of one or more of the figures in this paper are available online at http://ieeexplore.ieee.org.

Digital Object Identifier 10.1109/TPEL.2016.2616371

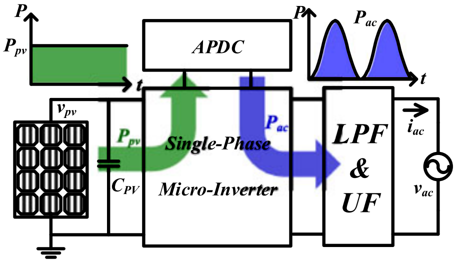

Fig. 2. Circuit configuration and corresponding power flows for WPPD strategy.

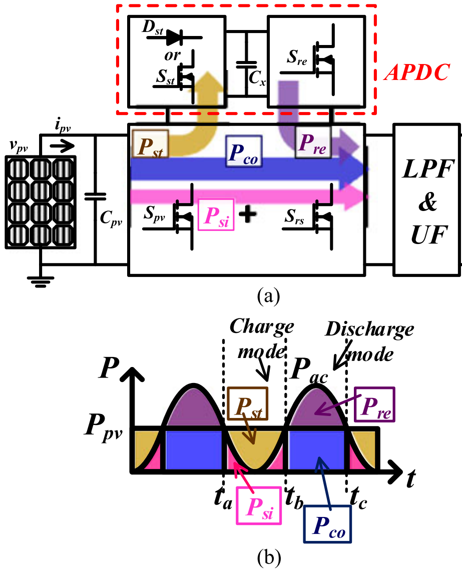

(a)

(b)

Fig. 3. PV micro-inverters with SPPD strategy. (a) Circuit configuration. (b) Corresponding power waveforms.

grid. To prevent the time-varied grid power affecting constant PV power delivering, the power difference between the input PV power and the output grid power, as marked by shaded area in Fig. 1(b), is usually decoupled by adding a large electrolytic capacitor at the input terminal of PV micro-inverter, as C_{PV} shown in Fig. 1(a). However, electrolytic capacitors have the drawback of short lifetime, especially under high temperature, and are not compatible with the lifetime of PV panel, usually guaranteed for 25 years. Therefore, many power decoupling techniques have been developed to reduce the required input capacitance so that the film capacitor with long lifetime can be used to decouple the power difference between the PV panel and the ac grid [17]–[34]. Besides, the MPPT performance and the lifetime of PV micro-inverter should remain unaffected under the usage of power decoupling techniques.

An active power decoupling circuit (APDC) is employed to fulfill the power decoupling technique for the PV micro-inverter. According to those published papers, the whole PV power decoupling (WPPD) and the sectional PV power decoupling (SPPD) are the two decoupling strategies to manipulate the power flow between the PV panel, the APDC, and the ac grid. For the WPPD strategy, where the corresponded power flow diagram is shown in Fig. 2, the APDC of PV micro-inverter will absorb whole constant PV power P_{PV}, which is indicated as the green line, and deliver sinusoidal power P_{ac}, which is indicated as the blue line, to the ac grid via the low-pass filter (LPF) and unfolder (UF) [17], [18]. Since the power flow operation is similar to the two-stage circuit operation and the full rated power will flow through the APDC, the power loss and the size of energy storage components will be increased.

For the SPPD strategy, the circuit configuration and corresponding power flows for the conventional PV micro-inverter with APDC is shown in Fig. 3(a) while the corresponding power waveforms are shown in Fig. 3(b). By adopting the APDC with SPPD strategy, the PV micro-inverters can achieve high MPPT performance without the need of electrolytic capacitors [19]–[34]. The constant power supplied by the PV panel is P_{PV} and the sinusoidal power injected into the ac grid via LPF and UF is P_{ac}. Two operation modes, the charge mode and the discharge mode, should be identified to achieve the power flow control.

During the charge mode, from t_a to t_b in Fig. 3(b), the constant PV power P_{PV} drawn from the PV panel by the switch S_{PV} is delivered either to the ac grid by the switch S_{rs} or to C_x by the diode D_{st} or the switch S_{st}. As the power flow shown in Fig. 3(a), $P_{\mathrm{PV}} = P_{\mathrm{st}} + P_{Si}$ and $P_{\mathrm{ac}} = P_{Si}$. The switch S_{re} inside the APDC is always off and no power flow is transferred from C_x to the ac grid.

For the discharge mode, between t_b and t_c in Fig. 3(b), P_{PV} is directly transferred from the PV panel to the ac grid by S_{PV} and S_{rs}. The insufficient power P_{re} is supplied from C_x to the ac grid by the switch S_{re}. That is, $P_{\mathrm{PV}} = P_{\mathrm{co}}$ and $P_{\mathrm{ac}} = P_{\mathrm{co}} + P_{\mathrm{re}}$. No PV power is delivered to C_x since the switch S_{st} keeps off.

Among the published papers with the SPPD strategy, the APDC, which is composed of boost converter with a synchronous switch, can be connected in parallel with the input battery source [19]. The power difference between the battery source and the ac grid is manipulated by the two switches, respectively, in charge mode and discharge mode. The input current ripple is reduced by the APDC and the lifetime of battery can be extended. In [20], an APDC, formed by an inductor, a capacitor, and a pair of back to back series-connected switches, is inserted into the converter with an additional transformer winding. The pair of switch operate in different modes to absorb or release power difference between the PV panel and the ac grid. In [25], an APDC is also attached to the additional transformer winding to decouple the mismatching power between the PV panel and the ac grid. However, no additional inductor is needed in the APDC since the decoupled power is transferred by the magnetizing inductor of transformer. In [28], the inductor is not required for the APDC neither. Different to [25], only the insufficient power is released from the APDC to the ac grid via the additional transformer winding in the discharge mode. A part of the PV power is directly stored into the APDC since it is connected to the PV panel. In [31], neither the inductor nor the additional transformer winding is utilized in the APDC. The circuit topology is simple and the component counts is reduced.

It is true that the APDC needs additional components to fulfill the desired function, and the overall system efficiency will be affected. However, many factors, such as the input/output voltage or the capacitance quantity, will affect the circuit operation and influence the converter's performance, eventually. Therefore, it is very difficult to find the efficiency trend with respect to the circuit topologies. For example, [25] has less component counts but the efficiency is only 73%. Also, [29] and [31] have the same power and voltage ratings but [29] has the higher efficiency with larger component counts.

Some series-type APDCs have been proposed to decouple the power between the PV panel and the ac grid [33]–[37]. In [33], the APDC is series connected between two converters to prevent the voltage ripple produced by one converter affecting the other one. No current sense is needed for the control of the APDC and good power decoupling performance can be achieved. Different from paper [33], the APDC in [36] is series connected with a capacitor to keep the voltage across dc-link capacitor constant. Maximum and constant power can thus be extracted from PV panel. In [37], a series-connected APDC is inserted between a full-bridge converter with a resonant tank and a cycloconverter. With the phase angle and on-time duration adjustment of the switches in the APDC, the mismatching power can be stored into or released from the APDC in charge or discharge mode, respectively.

The mismatching power between the PV panel and the ac grid of these published PV micro-inverters can therefore be decoupled by the sequence of power delivering in two operation modes. However, to distinguish the operation of charge or discharge mode in the conventional PV micro-inverter, the time points t_a, t_b, and t_c in Fig. 3(b), should be precisely determined by detecting the quantity of PV power and ac power or sensing the phase angle of ac voltage. More control design is needed for the APDC to determine the PV micro-inverter operation mode, either charging mode or discharging mode.

A novel topology with PV current decoupling (PVCD) strategy is proposed here for realization of the PV micro-inverter. The proposed PV micro-inverter can thus draw the maximum power from the PV panel and deliver a desired double-line frequency power into the ac grid without using electrolytic capacitors. Different to the conventional SPPD strategy, the proposed PVCD does not need to determine whether the PV micro-inverter should operate either in the charging mode or discharging mode. In this paper, the circuit diagram and the operation principle of proposed PV micro-inverter will be introduced. Then, the control block diagram of the proposed PVCD strategy will also be presented clearly followed by components design considerations. Finally, a 240 W prototype circuit will be built and tested. Computer simulation and experimental results will be shown to verify the performance of the proposed PV micro-inverter with PVCD strategy.

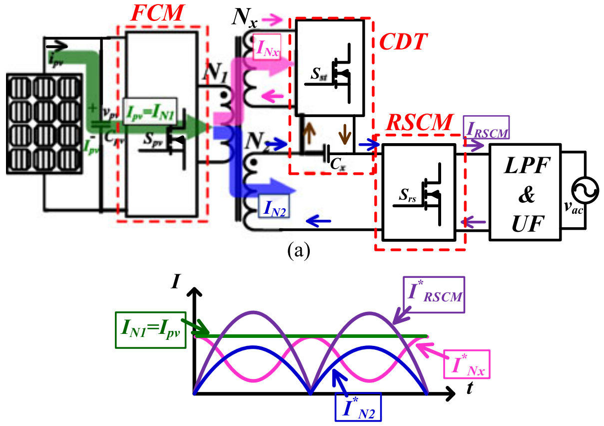

(a)

(b)

Fig. 4. Proposed PV micro-inverter with PVCD strategy. (a) The circuit configuration with current flow. (b) The corresponding current waveforms.

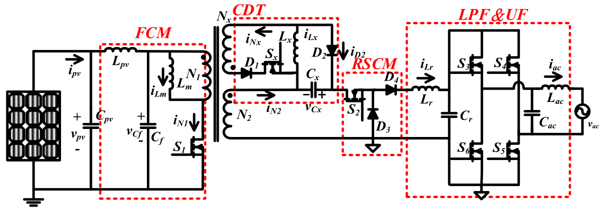

Fig. 5. Circuit topology of the proposed PV micro-inverter.

II. PROPOSED PV MICRO-INVERTER WITH PVCD STRATEGY

The conceptual circuit diagram of the proposed PV micro-inverter with PVCD strategy and its corresponding current waveforms are shown in Fig. 4(a) and (b), respectively. As shown in Fig. 4(a), by controlling the switch $S_{\rm rs}$ in the rectified sinusoidal current modulator (RSCM), the rectified sinusoidal current I_{N2} can be drawn from the energy source composed of the energy storage capacitor C_x and the transformer winding N_2. Then, a rectified sinusoidal current $I_{\rm RSCM}$, which is the output of the RSCM, will be converted into a sinusoidal one and injected into the ac grid by the UF and LPF. Meanwhile, by modulating the switch $S_{\rm st}$, the decoupling current I_{Nx} will flow through the current decoupling tank (CDT) to store charges, as well as energy, into C_x. As a result, the reflected I_{N2} and I_{Nx} on the primary side of the transformer, as illustrated by the current waveform I^*_{N2} and I^*_{Nx} in Fig. 4(b), will form a constant PV current $I_{\rm PV}$ if the switch $S_{\rm PV}$ in the fixed current modulator (FCM) is turned on along with the on state of the switches $S_{\rm rs}$ and $S_{\rm st}$. $I^*_{\rm RSCM}$ shown in Fig. 4 (b) is the reflected $I_{\rm RSCM}$ on the primary side of the transformer. It should be mentioned that those current waveforms shown in Fig. 4(b) are conceptual waveforms after using an LPF to smooth out their high-switching-frequency components.

Different from those PV micro-inverters with power decoupling techniques, the proposed PV micro-inverter with PVCD strategy is able to deal with the decoupling current and generate the rectified sinusoidal current at the same time to keep the PV current constant. Furthermore, no additional operation modes are needed to determine the charging or discharging status for C_x, so the controller design can be simplified.

A novel circuit topology to fulfill the proposed micro-inverter with PVCD strategy is depicted in Fig. 5 where the conceptual function blocks, as shown in Fig. 4(b), are marked by the red dash lines. The power switch S_x in CDT will fulfill the function of switch $S_{\rm st}$ in Fig. 4(b) and is in charge of drawing an appropriate decoupling current to keep a constant current flowing out of the PV panel to achieve good MPPT function. A rectified sinusoidal current is generated by the switch S_2 in the RSCM, which is equivalent to the switch $S_{\rm re}$ in Fig. 4(b). The switch

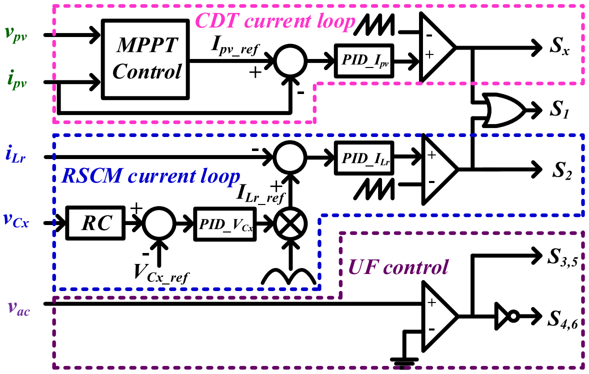

Fig. 6. Control block diagram of the proposed PV micro-inverter.

S_1 in FCM, like the switch $S_{\rm PV}$ in Fig. 4(b), is well controlled to ensure that the correct decoupling current flow and rectified sinusoidal current is draw from PV panel. The UF, which is formed by switches S_3–S_6, is operated with grid frequency to convert the rectified sinusoidal current into a pure sinusoidal one. Passive components, L_r, $L_{\rm ac}$, and $C_{\rm ac}$, form the LPF to attenuate the high-switchingfrequency current ripple to improve the injected current quality.

To achieve the desired MPPT and grid-connection functions for the proposed PV micro-inverter, the PVCD strategy based on the current decoupling instead of power decoupling is proposed. The control block diagram of the proposed PVCD strategy is shown in Fig. 6. It is mainly achieved by two current control loops, the RSCM current loop and the CDT current loop.

The average current mode control is adopted for the RSCM current loop to control the switch S_2 to generate the demanded rectified sinusoidal current. The current reference $I_{Lr\_{\rm ref}}$ is generated by a rectified sinusoidal signal, which is in phase with the grid voltage, multiplied by an amplitude factor, which is determined by the average voltage of C_x. A ripple cancellation (RC) function block is used to determine the average value of V_{Cx}, which will be compared to the reference one $V_{Cx\_{\rm ref}}$, to determine the amplitude of $I_{Lr\_{\rm ref}}$ and the injected ac grid-connected current. As the value of V_{Cx} increases/decreases, the amplitude of the injected ac grid-connected current will increase/decrease. The pulsewidth-modulated (PWM) gating signal of switch S_2 is generated by the average current mode control with a PID compensator *PID_ILr* for current i_{Lr} to trace the rectified sinusoidal current reference $I_{Lr\_{\rm ref}}$. Then, the control of switch pairs in UF will convert the rectified sinusoidal current, i_{Lr}, into a pure sinusoidal one $i_{\rm ac}$. During the positive half-cycle of the grid voltage, switch pairs S_3 and S_5 are turned on while S_4 and S_6 are turned off. On the other hand, S_3 and S_5 are off and S_4 and S_6 are on during the negative half-cycle.

For the CDT current loop, the PV reference current $I_{\rm PV\_ref}$ is generated by the MPPT control function. Theoretically, any MPPT control algorithm can be adopted to generate $I_{\rm PV\_ref}$. Due to its simplicity, the perturbation and observation (P&O) method is adopted to realize the MPPT control. By sensing the PV panel's voltage $v_{\rm PV}$ and current $i_{\rm PV}$, the MPPT controller will generate the reference current $I_{\rm PV\_ref}$, which is almost a constant quantity under a steady solar irradiation. Since the rectified sinusoidal current I_{Lr} is drawn from the PV panel, the decoupling current I_{Nx} will be drawn by the CDT with the control of the switch S_x when a constant PV current $i_{\rm PV}$ is well regulated with the PID compensator PID_*Ipv* to achieve the MPPT function.

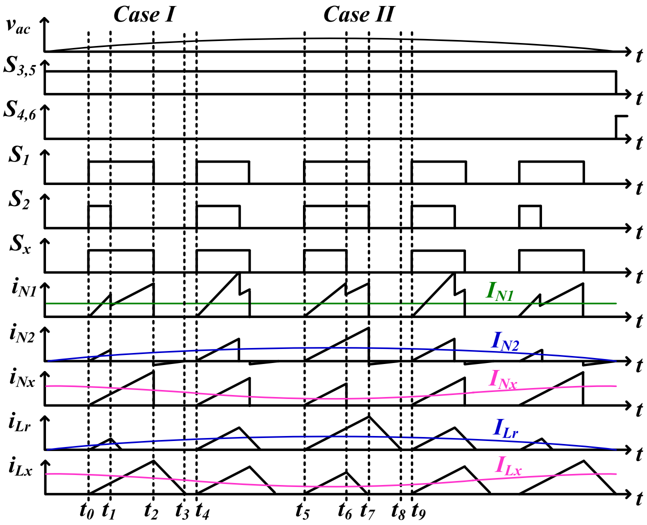

Fig. 7. Conceptual switch signals and current waveforms of the proposed PV micro-inverter with PVCD strategy.

On the other hand, whenever the PV current is transferred to the CDT or the RSCM when the switch S_x or S_2 is turned on, the switch S_1 should be turned on at the same time. Therefore, an OR gate is used to generate the gating signal for the switch S_1.

III. OPERATION PRINCIPLE OF PROPOSED PV MICRO-INVERTER

According to the circuit topology and the control block diagram mentioned in the previous section, the conceptual switch signals and current waveforms of the proposed PV micro-inverter with PVCD strategy are shown in Fig. 7. Since the circuit operation is the same during the positive or negative ac mains cycle, only the waveforms for the positive half-cycle are shown. The switches S_3 and S_5 in UF are fully turned on and S_4 and S_6 are fully turned off.

It should be mentioned that variables in uppercase letters represent the average values or the line frequency values while those ones in lowercase letters indicate the instantaneous values related to the switching frequency.

Depends on the on-time duration ($t_{{\rm on},S2}$ and $t_{{\rm on},Sx}$) of switch S_2 and S_x, the operation of the proposed PV micro-inverter can be divided into two cases: Case I ($t_{{\rm on},S2} < t_{{\rm on},Sx}$) and Case II ($t_{{\rm on},S2} > t_{{\rm on},Sx}$). Furthermore, by comparing to the continuous conduction mode (CCM) current operation of inductors L_r and L_x, the discontinuous conduction mode (DCM) operation of the two inductors has more operation situations. Therefore, by considering the DCM operation of L_r and L_x, six operation stages are distinguished during the positive half-cycle of the grid voltage. Detailed circuit operation and current flow will be described as follows:

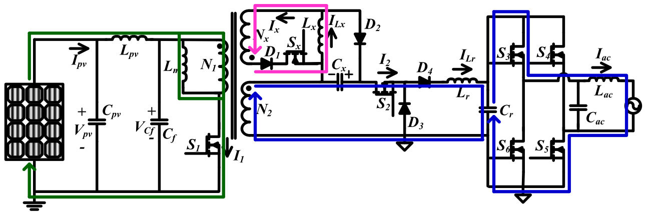

Fig. 8. Delivering PV current to L_{x} and L_{r} simultaneously in Stage I.

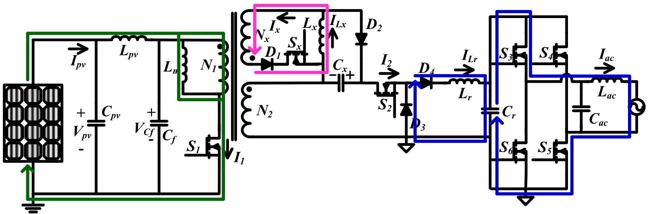

Fig. 9. Delivering PV current to L_x and releasing i_{Lr} to ac grid in Stage II.

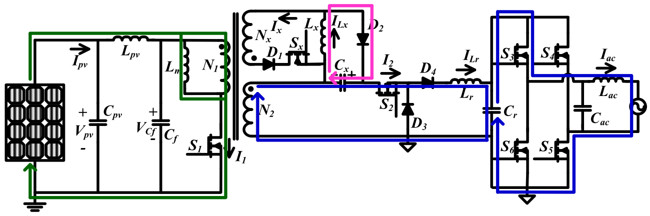

Fig. 10. Delivering PV current to L_r and releasing i_{Lx} to C_x in Stage III.

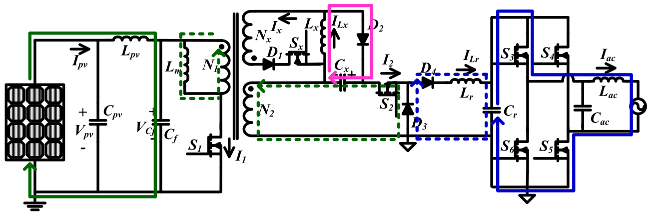

Fig. 11. Current i_{Lx} charges C_x while current i_{Lr} releases to C_{r} or drops to zero in Stage IV(a).

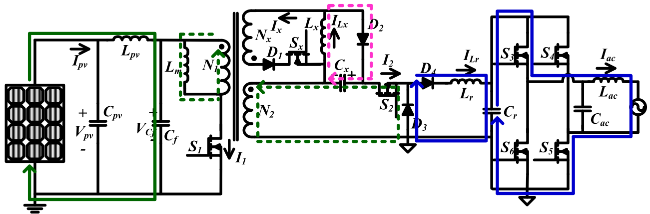

Fig. 12. Current i_{Lr} releases to C_r while current i_{Lx} charges C_x or drops to zero in Stage IV(b).

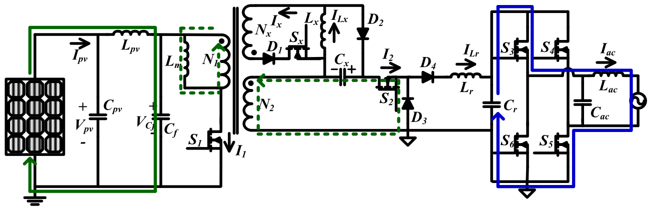

Fig. 13. Inductor currents i_{Lx} and i_{Lr} are zero in Stage IV(c).

1) Stage I $(\mathrm{t}_0 - \mathrm{t}_1$ *and* $t_5 - t_6)$*:* During this operation stage, all the switches S_1, S_2, and S_x are turned on. Currents i_{N1}, i_{N2}, i_{Nx}, i_{Lr}, and i_{Lx} are increased linearly, as shown in Fig. 7. The equivalent circuit with corresponding current paths are shown in Fig. 8. Energy storage capacitor C_x is in series with the transformer winding N_2 to deliver the current I_{N2} to the LPF and UF. At the same time, the decoupling current I_{Nx} is drawn from the PV panel into the CDT to store energy and charges inside the inductor L_x. A small portion of PV energy would also be charged into the magnetizing inductor L_m of transformer because of the on state of the switch S_1. Stage I ends when either one of the switches S_2 or S_x is turned off.

2) Stage II $(\mathrm{t}_1 - t_2)$*:* When the inductor current i_{Lr} in the RSCM current loop, as shown in Fig. 6, reach the desired current value I_{Lr_ref}, the switch S_2 will be turned off and the operation enter Stage II. The equivalent circuit with corresponding current paths of Stage II are shown in Fig. 9. Because S_2 is turned off, the freewheeling diode D_3 will be on and the inductor current i_{Lr} is, therefore, decreased. In the CDT current loop, as shown in Fig. 6, since the PV current i_{PV} has not yet achieved the desired reference current $I_{\mathrm{PV}\_\mathrm{ref}}$, the switches S_1 and S_x remain on and currents i_{N1} and i_{Nx} continue to increase. The magnetizing inductor current i_{Lm} continues to increase in this stage since the switch S_1 is still on.

3) Stage III $(\mathrm{t}_6 - t_7)$*:* On the other hand, if PV current i_{PV} reaches the reference current $I_{\mathrm{PV}\_\mathrm{ref}}$ in CDT current loop but inductor current i_{Lr} has not arrived the desired current reference I_{Lr_ref} in RSCM current loop, the switch S_x will be turned off while the switch S_1 and S_2 keep conducting, as shown in Fig. 10. It should be mentioned that Stage I is followed by either Stage II or Stage III so two operation cases are identified. During Stage III, the energy and charges stored in the inductor L_x are released to the decoupling capacitor C_x via the diode D_2 and inductor current i_{Lx} is thus decreased in this stage. Since the switches S_1 and S_2 are turned on, the energy of inductor L_r will be continuously charged by PV panel and its current i_{Lr} is increased reasonably. Similar to Stage II, the magnetizing inductor current i_{Lm} will continue to increase due to the on state of the switch S_1.

4) Stage IV(a)$(t_2 - t_3)$*:* After Stage II or Stage III, if the increasing PV current i_{PV} or inductor current i_{Lr} reaches its reference current, the corresponding switch S_x or S_2 will be turned off. Since both gate signals of S_2 and S_x are low, switch S_1 will be turned off, too. All switches S_1, S_2, and S_x are turned off and the operation mode becomes Stage IV. However, according to the discharging current in the inductor L_x and L_r, Stage IV should be further dived into three different modes, Stage IV(a), Stage IV(b), and Stage IV(c).

It should be mentioned that the dash current path in Figs. 11, 12, and 13 means the current keeps at zero value or is discharged to zero during the operation stage.

In Stage IV(a), as shown in Fig. 11, the decoupling capacitor C_x in the CDT is charged by the energy of inductor L_x via the diode D_2 and the energy of inductor L_r would be discharged

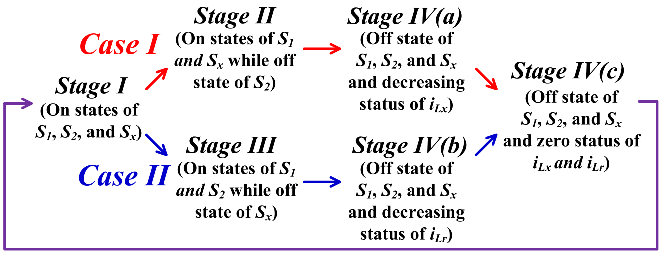

Fig. 14. Two cases of operation stages for the proposed PV micro-inverter.

to ac grid through the freewheeling diode D_3. However, the inductor current i_{Lr} will be discharged to zero before the inductor current i_{Lx} does. Then, the injected ac current will flow through the capacitor C_r. Since the switch S_1 is turned off, the PV current begins to charge the capacitor C_f and the energy of magnetizing inductor is released to C_x via the body diodes of switch S_2 and the diode D_3 until the magnetizing inductor current i_{Lm} is decreased to zero.

5) Stage IV(b)$(t_7 - t_8)$*:* Similar to Stage IV(a), if the inductor current i_{Lx} drops to zero before the inductor current i_{Lr} does, the operation becomes Stage IV(b), as shown in Fig. 12. Also, the energy of magnetizing inductor charges C_x if the magnetizing inductor current i_{Lm} is not decreased to zero during the off status of switch S_1.

6) Stage IV(c) $(t_3 - t_4$ *and* $t_8 - t_9)$*:* As both of the inductor current i_{Lx} and i_{Lr} decrease to zero, the circuit operation enters Stage IV(c). As the equivalent circuit with corresponding current path shown in Fig. 13, the PV current continues to flow into capacitors C_f and the injected ac current flows through the capacitor C_r. Before the magnetizing inductor current i_{Lm} is decreased to zero, the energy of magnetizing inductor L_m will continue to charge decoupling capacitor C_x.

With the above mentioned six stages, the proposed PV micro-inverter has two different operation cases. The Case I occurs during the time interval when grid voltage/current is relatively small while Case II appears at relatively larger grid voltage/current. Each case contains four operation stages, which appears in the sequence, as shown in Fig. 14.

In Case I, most of the PV current is delivered to the CDT while a relatively small current I_{Lr} is drawn to the RSCM since small grid ac current i_ac is demanded. The on-time of the switch S_x, which is generated by the CDT current loop, is therefore larger than that of the switch S_2, which is adjusted by the RSCM current loop. Consequently, Case I begins with Stage I, where all the switches S_1, S_2, and S_x are turned on. Then, Stage II, where the switches S_1 and S_x are turned on while S_2 is turned off, is followed. Next, the operation turns to Stage IV(a), where all the switches S_1, S_2, and S_x are turned off and inductor current i_{Lx} keeps decreasing while inductor current i_{Lr} is reduced to zero or has been zero. Finally, when i_{Lx} drops to zero, the operation enters Stage IV(c) and inductor current i_{Lx} and i_{Lr} keep at zero value. After Stage IV(c), the operation will go back to Stage I for a new switching cycle.

On the other hand, the on time of switch S_2 will be larger than that of the switch S_x when a large grid ac current i_ac is demanded. Therefore, the sequence of operation is similar to that in Case I except that Stage II and Stage IV(a) are replaced by Stage III and Stage IV(b), respectively, as shown in Fig. 14.

IV. CIRCUIT COMPONENTS DESIGN

In addition to the proposed PVCD strategy, circuit components design is also a very important task to ensure the correct operation of the proposed PV micro-inverter. In the following, important methodical equations for operation conditions, such as the turn-on time of the power switch or the transformer's current, will be derived first. Then, the design guidelines for key components will be presented. Finally, the selection criteria of active power devices based on the voltage stress are suggested.

Since the inductor L_r of the proposed PV micro-inverter can be operated in either CCM or DCM, the derived key equations shown in Table I are divided into two parts. First of all, based on the volt-second balance theory for the steady-state operation of the inductor L_r, the expression of (1.a) and (1.b) can be obtained, where $t_{\mathrm{off,dis},S2}$ is the discharged time of inductor L_r under DCM current operation. Then the on-time of the switch S_2, which is indicated as $t_{\mathrm{on},S2}$, can be derived as (2.a) and (2.b), where V_PV is the average voltage of PV panel, and $v_{Cx}(t)$ is the instantaneous voltage of C_x. $|v_\mathrm{ac}(t)|$ is the absolute value of instantaneous grid voltage. T_s is the switching period. N_1 and N_2 are the primary-side and secondary-side turns number of the transformer. In steady-state, the inductor current I_Lr should be equal to the absolute value of ac line current injected into the grid, so (3.a) and (3.b) can be obtained. By rearranging (3.a) and (3.b), the valley value, $I_{Lr,\mathrm{vy}}(t)$, and the peak value, $I_{Lr,\mathrm{pk}}(t)$, of instantaneous inductor current $i_{Lr}(t)$ can be expressed in (4.a) and (4.b). Therefore, the current of the transformer's secondary-winding, $I_{N2}(t)$, is expressed as (5.a) and (5.b), where I_PV is the average value of PV current and ω_ac is the grid angular frequency. It should be mentioned that the derived equations for $I_{N2}(t)$ under the DCM or CCM operation of L_r are expected to be identical since the same rectified sinusoidal current is drawn from the PV panel.

Similar to inductor L_r, inductor L_x can be designed to operate in DCM or CCM, so the derived key equations are shown in Table II. As shown in (6), to realize the PVCD strategy and keep the PV current constant, the decoupling current I_{Nx}, which is the difference between the primary-side and secondary-side transformer currents, should be draw into the CDT by the controlling of the switch S_x. According to the volt-second balance theory for the steady-state operation of the inductor L_x, (7.a) and (7.b) can be derived. The on-time of switch S_x, $t_{\mathrm{on},Sx}$, can be expressed as (8.a) and (8.b) while the decoupling current I_{Nx} is determined by (6). In Table II, N_x represents the turns number of CDT-side transformer winding and $t_{\mathrm{off,dis},Sx}$ is the discharged time of inductor L_x under DCM current operation. I_PV stands for the PV output current, which is equal to the primary-side transformer's current without considering switching-ripple current. The results of diode current $I_{D2}(t)$ can be expected to be identical, as shown in (9.a) and (9.b), while the same decoupling current I_{Nx} delivers to the decoupling capacitor C_x through the diode D_2 under the CCM or DCM operation of inductor L_x.The mathematical expression of the voltage, $v_{Cx}(t)$, for the

TABLE I
KEY EQUATIONS UPON THE CCM OR DCM OPERATION OF L_r

CCM Operation		DCM Operation	
$\left(\frac{N_2}{N_1}\cdot V_{\rm PV}+v_{Cx}(t)-\lvert v_{\rm ac}(t)\rvert\right)t_{{\rm on},S2}=\lvert v_{\rm ac}(t)\rvert\cdot(T_s-t_{{\rm on},S2})$	(1.a)	$\left(\frac{N_2}{N_1}\cdot V_{\rm PV}+v_{Cx}(t)-\lvert v_{\rm ac}(t)\rvert\right)t_{{\rm on},S2}=\lvert v_{\rm ac}(t)\rvert t_{{\rm off,dis},S2}$	(1.b)
$t_{{\rm on},S2}=\frac{\lvert v_{\rm ac}(t)\rvert\cdot T_s}{\frac{N_2}{N_1}\cdot V_{\rm PV}+v_{Cx}(t)}$	(2.a)	$t_{{\rm on},S2}=\frac{\lvert v_{\rm ac}(t)\rvert}{\frac{N_2}{N_1}\cdot V_{\rm PV}+v_{Cx}(t)-\lvert v_{\rm ac}(t)\rvert}t_{{\rm off,dis},S2}$	(2.b)
$\frac{1}{2}\cdot\frac{\lvert v_{\rm ac}(t)\rvert}{L_r}(T_s-t_{{\rm on},S2})+I_{Lr,{\rm vy}}(t)=\lvert i_{\rm ac}(t)\rvert$	(3.a)	$\frac{1}{T_s}\cdot\frac{1}{2}\cdot(t_{{\rm on},S2}+t_{{\rm off,dis},S2})\cdot I_{Lr,{\rm pk}}(t)=\lvert i_{\rm ac}(t)\rvert$	(3.b)
$I_{Lr,{\rm vy}}(t)=\lvert i_{\rm ac}(t)\rvert-\frac{1}{2}\cdot\frac{\lvert v_{\rm ac}(t)\rvert}{L_r}(T_s-t_{{\rm on},S2})$	(4.a)	$I_{Lr,{\rm pk}}(t)=\frac{2T_s\cdot\lvert v_{\rm ac}(t)\rvert\cdot\lvert i_{\rm ac}(t)\rvert}{\left(\frac{N_2}{N_1}\cdot V_{\rm pv}+v_{Cx}(t)\right)\cdot t_{{\rm on},S2}}$	(4.b)
$I_{N2}(t)=\frac{1}{2}\cdot[2\cdot I_{Lr,{\rm vy}}(t)+\frac{\lvert v_{\rm ac}(t)\rvert}{L_r}\cdot(T_s-t_{{\rm on},S2})]\cdot t_{{\rm on},S2}$ $=\lvert i_{\rm ac}(t)\rvert\cdot t_{{\rm on},S2}=\frac{V_{\rm pv}I_{\rm pv}\cdot(1-\cos(2\omega_{\rm ac}t))}{\frac{N_2}{N_1}\cdot V_{\rm pv}+v_{Cx}(t)}$	(5.a)	$I_{N2}(t)=\frac{1}{T_s}\cdot\frac{1}{2}\cdot t_{{\rm on},S2}\cdot I_{Lr,{\rm pk}}(t)$ $=\frac{V_{\rm PV}I_{\rm PV}\cdot(1-\cos(2\omega_{\rm ac}t))}{\frac{N_2}{N_1}\cdot V_{\rm PV}+v_{Cx}(t)}$	(5.b)

TABLE II
KEY EQUATIONS UPON THE CCM OR DCM OPERATION OF L_x

CCM Operation		DCM Operation	
$I_{Nx}(t)=\frac{N_1}{N_x}\cdot I_{\rm PV}-\frac{N_2}{N_x}\cdot I_{N2}(t)$			(6)
$\frac{N_x}{N_1}\cdot V_{\rm PV}\cdot t_{{\rm on},Sx}=v_{Cx}(t)\cdot(T_s-t_{{\rm on},Sx})$	(7.a)	$\frac{N_x}{N_1}\cdot V_{\rm PV}\cdot t_{{\rm on},Sx}=v_{Cx}(t)\cdot t_{{\rm off,dis},Sx}$	(7.b)
$t_{{\rm on},Sx}=\frac{v_{Cx}(t)\cdot T_s}{\frac{N_x}{N_1}\cdot V_{\rm PV}+v_{Cx}(t)}$	(8.a)	$t_{{\rm on},Sx}=\frac{v_{Cx}(t)}{V_{\rm PV}}\cdot\frac{N_1}{N_x}\cdot t_{{\rm off,dis},Sx}$	(8.b)
$I_{D2}(t)=I_{Nx}(t)\cdot\left(\frac{T_s-t_{{\rm on},Sx}}{t_{{\rm on},Sx}}\right)$ $=\frac{\frac{N_x}{N_1}\cdot V_{\rm PV}}{v_{Cx}(t)}\cdot I_{Nx}(t)$	(9.a)	$I_{D2}(t)=\frac{1}{T_s}\cdot\frac{1}{2}\cdot\frac{v_{Cx}(t)}{L_x}\cdot t^2_{{\rm off,dis},Sx}$ $=\frac{\frac{N_x}{N_1}\cdot V_{\rm PV}}{v_{Cx}(t)}\cdot I_{Nx}(t)$	(9.b)

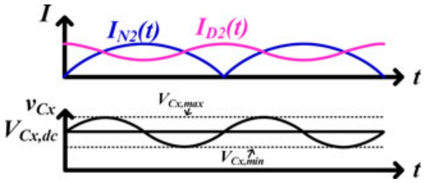

Fig. 15. Corresponding waveforms of I_{D2}, I_{N2}, and v_{Cx}.

decoupling capacitor C_x can be established by determining its current first. According to the circuit diagram shown in Fig. 5, the capacitor current $i_{Cx}(t)$ is the difference between the current I_{D2} on diode D_2 and the transformer current I_{N2}. By combining (5.b), (6), and (9.b), the mathematical expression of capacitor current $i_{Cx}(t)$ can be obtained as (10). Then, by solving the differential (10), the mathematical expression of the voltage, $v_{Cx}(t)$, for the decoupling capacitor C_x can be obtained, as shown in (11). The corresponding waveforms of I_{D2}, I_{N2}, and $v_{Cx}(t)$ after an LPF are shown in Fig. 15, where $V_{Cx,\rm dc}$ is the average value of $v_{Cx}(t)$

$$\begin{aligned} C_x\cdot\frac{dv_{Cx}(t)}{dt} &= i_{Cx}(t)=I_{D2}(t)-I_{N2}(t)\\ &= \frac{V_{\rm PV}\cdot I_{\rm PV}}{v_{Cx}(t)}\cdot\cos\left(2\omega_{\rm ac}t\right) \end{aligned} \tag{10}$$

$$v_{Cx}(t)=\sqrt{\frac{P_{\rm PV}}{\omega_{\rm ac}\cdot C_x}\sin(2\omega_{\rm ac}t)+V^2_{Cx,\rm dc}}. \tag{11}$$

Based on the derived equations mentioned earlier, key component design rules can be established as follows.

A. Decoupling Capacitor $C_{\rm x}$ and Turns Ratio $\rm N2/N1$

As shown in Fig. 15, the voltage ripple of $v_{Cx}(t)$, ΔV_{Cx}, is determined by the difference between the maximum value $V_{Cx,\max}$ and the minimum value $V_{Cx,\min}$. From (11), the value of ΔV_{Cx} can be expressed as

$$\begin{aligned} \Delta V_{Cx} = V_{Cx,\max}-V_{Cx,\min} &= \sqrt{V^2_{Cx,\rm dc}+\frac{P_{\rm PV}}{\omega_{\rm ac}\cdot C_x}}\\ &\quad -\sqrt{V^2_{Cx,\rm dc}-\frac{P_{\rm PV}}{\omega_{\rm ac}\cdot C_x}}. \end{aligned} \tag{12}$$

Assuming a rated $P_{\rm PV}$ with a constant $\omega_{\rm ac}$, Fig. 16 shows the curves of the required decoupling capacitance C_x under different demanded voltage ripple ΔV_{Cx} and dc voltage $V_{Cx,\rm dc}$ values. As the values of ΔV_{Cx} and $V_{Cx,\rm dc}$ decreased, the required decoupling capacitance C_x should be increased. Also, a larger C_x is needed for a higher rated $P_{\rm PV}$. In practical, the values of $P_{\rm PV}$, ΔV_{Cx}, and $V_{Cx,\rm dc}$ should be decided first, then

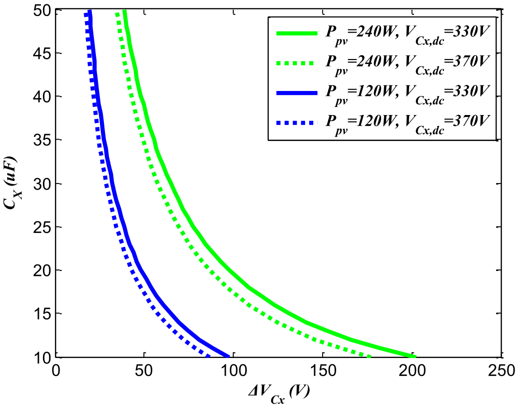

Fig. 16. Required decoupling capacitance C_x for different ΔV_{Cx} and $V_{Cx,\mathrm{dc}}$ values.

the capacitor value of C_x could be easily obtained from (12) or Fig. 16.

It should be mentioned that the required decoupling capacitance C_x for different ΔV_{Cx} and $\Delta V_{Cx,\mathrm{dc}}$ values are similar to those of other publised topologies. It is understandable that the required decoupling capacitance in the proposed topology should be similar to those ones in the published papers since the same amount of mismatch power between the PV panel and the ac mains should be buffered by the decoupling capacitor. In addition to providing the information for component design, the derived equation of the required decoupling capacitance also reveal the correctness of the proposed PVCD technique.

To deliver PV current to the UF and LPF, the transformer's turns ratio N_1/N_2 needs to be designed appropriately. As shown in Fig. 5, when both switches S_1 and S_2 are turned on, the voltage across on diode D_3, which is the summation of the reflected PV voltage on the transformer's secondary side and the decoupling voltage v_{Cx}, should be larger than the peak voltage $V_{Cr,\mathrm{pk}}$ on C_r. Therefore, the following equation can be obtained:

$$\frac{N_2}{N_1} \cdot V_{\mathrm{PV,min}} + V_{Cx,\min} \geq V_{Cr,\mathrm{pk}}. \tag{13}$$

where $V_{\mathrm{PV,min}}$ is the minimum PV voltage value and $V_{Cr,\mathrm{pk}}$ is the peak value of capacitor voltage of C_r. From (13), when $V_{\mathrm{PV,min}}$, $V_{Cx,\min}$, and $V_{Cr,\mathrm{pk}}$ are decided, the proper turns ratio N_2/N_1 could be figure out.

B. Inductor L_r, L_{ac}, and Capacitor C_r, C_{ac}

The equivalent circuit of UF and LPF can be redrawn and shown in Fig. 17, where the LPF is formed by L_r, C_r, L_{ac}, and C_{ac}. Because of the nature of switching converter, ripple current appears on L_r should be attenuated by the LPF while injecting the current into the grid. Assuming a negligible switching-frequency ripple voltage on C_r, the expression of ripple current of inductor L_r Δi_{Lr} can be shown in (14.a), where $\Delta i_{Lr,\min}$ is the predetermined boundary condition for the CCM operation. When the switch S_2 is turned off, the current of inductor L_r will be discharged. The time for the inductor current i_{Lr} to discharged to zero is denoted as $t_{\mathrm{off,dis},S2}$. For the DCM operation, (14.b) must be satisfied. By combining (14.a) and (14.b), the required inductance L_r for CCM or DCM operation can be expressed as (15.a) and (15.b), respectively.

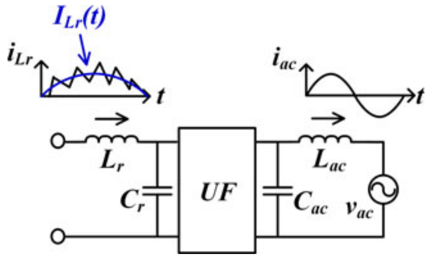

Fig. 17. Equivalent circuit of UF and LPF, which is formed by L_r, C_r, C_{ac}, and L_{ac}.

TABLE III
EQUATIONS FOR L_r DESIGN

CCM Operation		DCM Operation	
$\frac{\lvert v_{\mathrm{ac}}(t)\rvert}{L_r} \cdot (T_s - t_{\mathrm{on},S2})$ $= \Delta i_L r \leq \Delta i_L r,\min$	(14.a)	$t_{\mathrm{on},S2} + t_{\mathrm{off,dis},S2}$ $\leq T_s$	(14.b)
$L_r \geq \frac{T_s \cdot \lvert v_{\mathrm{ac}}(t)\rvert}{\Delta i_L r,\min}$ $\left(1 - \frac{\lvert v_{\mathrm{ac}}(t)\rvert}{\frac{N_2}{N_1} \cdot V_{\mathrm{PV}} + v_{Cx}(t)}\right)$	(15.a)	$L_r \leq \frac{T_s \cdot \lvert v_{\mathrm{ac}}(t)\rvert}{2 \cdot \lvert i_{\mathrm{ac}}(t)\rvert} \cdot$ $\left(1 - \frac{\lvert v_{\mathrm{ac}}(t)\rvert}{\frac{N_2}{N_1} \cdot V_{\mathrm{PV}} + v_{Cx}(t)}\right)$	(15.b)

It should be mentioned that (15.a) and (15.b) become the same when $\Delta i_{Lr,\min}$ is designed to be twice of the absolute value of grid current $i_{\mathrm{ac}}(t)$.The result is similar to the design for the CCM or DCM operation of the dc–dc buck converter.

The other components inside the LPF form an LPF to smooth out the injected ac current. The transfer function of the LPF, which consists of C_r, C_{ac}, and L_{ac}, can be obtained:

$$\frac{\Delta i_{\mathrm{ac}}}{\Delta i_{Lr}} = \frac{1}{1 + \omega_{c,\mathrm{ac}}^2 \left[L_{\mathrm{ac}}\left(C_r + C_{\mathrm{ac}}\right)\right]} \tag{16}$$

where Δi_{ac} is the switching-frequency current ripple of injected ac current and $\omega_{c,\mathrm{ac}}$ is the corner angular frequency of the LPF. Generally, $\omega_{c,\mathrm{ac}}$ is designed to be one-tenth of the switching angular frequency. After the ratio of current ripple of Δi_{Lr} to Δi_{ac} is decided, the value of L_{ac}, C_r, and C_{ac} can be determined.

C. Inductor L_{x} and Turns Ratio N_{x}/N_1

Similar to the inductor L_r, the derived equation for inductor L_{x} to operate in CCM or DCM are shown in Table IV, where Δi_{Lx} is the ripple current of L_x, $\Delta i_{Lx,\min}$ is the predetermined boundary current, and $t_{\mathrm{off,dis},Sx}$ is the time for inductor current to discharge to zero during the off time of the switch S_x. Also, $I_{Lx}(t)$ is the current of inductor L_x without considering its switching ripple current. Similar to the conditions shown in Table III, (18.a) and (18.b) in Table IV are expected to be the same when $\Delta i_{Lx,\min}$ is designed equally to be twice of inductor current $I_{Lx}(t)$, which is the design criteria for the CCM or DCM operation of the dc–dc buck–boost converter.

TABLE IV
EQUATIONS FOR L_x DESIGN

CCM Operation		DCM Operation	
$\frac{v_{C\,x}(t)}{L_x}\cdot(T_s - t_{\text{on},S\,x}) = \Delta i_{L\,x} \leq \Delta i_L\, x, \min$	(17.a)	$t_{\text{on},S\,x} + t_{\text{off,dis},S\,x} \leq T_s$	(17.b)
$L_x \geq \frac{T_s \cdot v_{C\,x}(t)}{\Delta i_L\, x, \min}\cdot\left(1 - \frac{v_{C\,x}(t)}{\frac{N_x}{N_1}\cdot V_{\text{PV}} + v_{C\,x}(t)}\right)$	(18.a)	$L_x \leq \frac{T_s \cdot v_{C\,x}(t)}{2\cdot I_{L\,x}(t)}\cdot\left(1 - \frac{v_{C\,x}(t)}{\frac{N_x}{N_1}\cdot V_{\text{PV}} + v_{C\,x}(t)}\right)$	(18.b)

D. Input Filter L_{PV}, C_{PV}, and C_{f}

To achieve good MPPT performance, the input filter, which consists of inductor L_{PV} and capacitors C_{PV} and C_f, should be carefully designed to attenuate the switching ripple on the PV panel. The required capacitance C_f is related to the PV current I_{PV}, voltage ripple Δv_{Cf} on the capacitor C_f, switching period T_s, and the on-time of the switch S_1. As a result, the minimum value of the required capacitor $C_{f,\min}$ can be expressed as

$$C_{f,\min} \geq \frac{I_{\text{PV}}}{\Delta v_{Cf}}\left(T_s - t_{\text{on},S1,\min}\right). \tag{19}$$

where $t_{\text{on},S1,\min}$ is the minimum on-time of the switch S_1. On the other hand, L_{PV} and C_{PV} form an LPF to further reduce the switching voltage ripple on the PV panel. The attenuation ratio of the LPF can be expresses as

$$\frac{\Delta v_{\text{PV}}}{\Delta v_{Cf}} = \frac{1}{1 + \omega_{c,\text{PV}}^2 L_{\text{PV}} C_{\text{PV}}} \tag{20}$$

where Δv_{PV} represents the voltage ripple of PV panel and $\omega_{c,\text{ PV}}$ is demanded corner frequency of the LPF. Similar to $\omega_{c,\text{ ac}}$, $\omega_{c,\text{ PV}}$ is also designed to be one tenth of the switching angular frequency. Once the attenuation ratio of the voltage ripple is decided, the value of L_{PV} and C_{PV} can be determined.

E. Voltage Stress of Power Devices

The voltage stress for power switches S_1, S_2, and S_x can be determined by their operation modes. As the equivalent circuits in Figs. 11 and 12, the maximum voltage stress of S_1 $V_{\text{DS},\,S1,\,\max}$ occurs when both S_2 and S_x are off but the body diode of S_2 and diode D_3 are conducting due to the discharging of magnetizing current of L_m. Therefore, the voltage stress of S_1 can be expressed as

$$V_{\text{DS},S1,\max} = V_{\text{PV}} + V_{Cx,\max}\cdot\frac{N_1}{N_2} \tag{21}$$

where $V_{Cx,\max}$ is the maximum voltage of capacitor C_x.

When switch S_2 is turned off in Fig. 9, the diode D_3 will be turned on because of the continuity of the inductor current i_{Lr}. Therefore, the maximum voltage stress of switch S_2 $V_{\text{DS},\,S2,\,\max}$ becomes the summation of the transformer winding voltage and the maximum voltage of capacitor C_x while the switch S_1 is turned on and can be expressed as (22). Similarly, the maximum voltage stress of switch S_x $V_{\text{DS},\,Sx,\,\max}$ can be determined and shown in (23)

$$V_{\text{DS},S2,\max} = V_{\text{PV}}\cdot\frac{N_2}{N_1} + V_{Cx,\max} \tag{22}$$

$$V_{\text{DS},Sx,\max} = V_{\text{PV}}\cdot\frac{N_x}{N_1} + V_{Cx,\max}. \tag{23}$$

The maximum voltage on diode D_1 happens when magnetizing inductor current i_{Lm} is discharged and inductor current i_{Lx} is dropped to zero during the off status of switches S_1, S_2, and S_x, such as the equivalent circuit in Fig. 12. Because of the body diode of S_x, the voltage of transformer winding N_x will across on the diode D_1. Therefore, the maximum voltage stress of diode D_1 $V_{D1,\,\max}$ becomes

$$\text{V}_{D1,\max} = V_{Cx,\max}. \tag{24}$$

The diodes D_2 and D_3 will be reversely biased, while switches S_x and S_2 are turned on, respectively, in Fig. 8. Therefore, the maximum blocking voltage on these two diodes $V_{D2,\,\max}$ and $V_{D3,\,\max}$ can be obtained

$$V_{D2,\max} = V_{\text{PV}}\cdot\frac{N_x}{N_1} + V_{Cx,\max} \tag{25}$$

$$V_{D3,\max} = V_{\text{PV}}\cdot\frac{N_2}{N_1} + V_{Cx,\max}. \tag{26}$$

On the other hand, the switching pairs $(S_3,\, S_5)$ and $(S_4,\, S_6)$ in UF are turned on complementary during the positive or negative half-cycle of the grid voltage. Therefore, the maximum blocking voltage for each switch in one switching pair is the peak ac voltage $v_{\text{ac, pk}}$ while the other switching pair is turned on and can be expressed as

$$V_{S3,\max} = V_{S4,\max} = V_{S5,\max} = V_{S6,\max} = v_{\text{ac, pk}}. \tag{27}$$

V. SIMULATION AND EXPERIMENTAL RESULTS

A prototype circuit with the specifications shown in Table V is built and tested to verify the performance of the proposed PV micro-inverter with PVCD strategy. It should be mentioned that no electrolytic capacitor is needed for the hardware implementation. Computer simulation key waveforms for the proposed PV micro-inverter are shown in Fig. 18, where from top to bottom are PV voltage v_{PV}, PV current i_{PV}, ac grid voltage v_{ac}, ac grid current i_{ac}, decoupling capacitor voltage v_{Cx}, and magnetizing current i_{Lm}. It can be seen that both v_{PV} and i_{PV} are almost constant, which implies that the PV panel provides a constant power and good MPPT performance is achieved. The injected

TABLE V
SPECIFICATIONS OF THE PROPOSED PV MICRO-INVERTER

Parameter	Value	Parameter	Value
$V_{\mathrm{PV,mpp}}$	30 V	L_{PV}	10 μH
$I_{\mathrm{PV,mpp}}$	8 A	C_f	47 μF
$P_{\mathrm{PV,mpp}}$	240 W	C_x	25 μF
V_{ac}	220 $\mathrm{V_{rms}}$	C_r	50 nF
f_{ac}	60 Hz	L_x	250 μH
f_{sw}	50 kHz	L_r	600 μH
C_{PV}	7 μF	L_{ac}	2 mH
$N_1 : N_x : N_2$	1:3.5:3.5	C_{ac}	50 nF

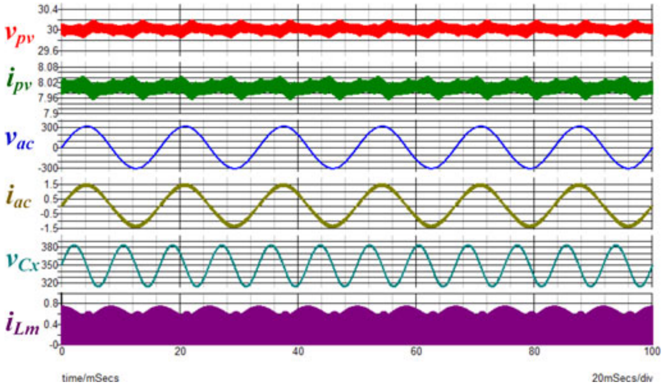

Fig. 18. Simulation key waveforms for steady state operation with rated PV power.

ac line i_{ac} is sinusoidal and is in phase with the grid voltage v_{ac}. The average value of the decoupling capacitor C_x, v_{Cx}, is well controlled at 350 V with a reasonable double-line frequency voltage ripple around 70 V appearing. Thus, the input and output currents are decoupled successfully. In addition, due to the discharging path inside the proposed PV micro-inverter, the magnetizing inductor current i_{Lm} can always be discharged to zero in every switching cycle to recycle the magnetic energy as well as to avoid the transformer saturation.

On the other hand, simulated gating signals and corresponding current waveforms for Case I and Case II are shown in Fig. 19(a) and (b), respectively. In Fig. 19, waveforms from top to bottom are line voltage v_{ac}, gating signal of S_1, S_x, and S_2, and the current waveforms for i_{Lx} and i_{Lr}. These simulated waveforms are consistent with the theoretical ones shown in Fig. 7 that validate the operation principle of the proposed PV micro-inverter with PVCD strategy.

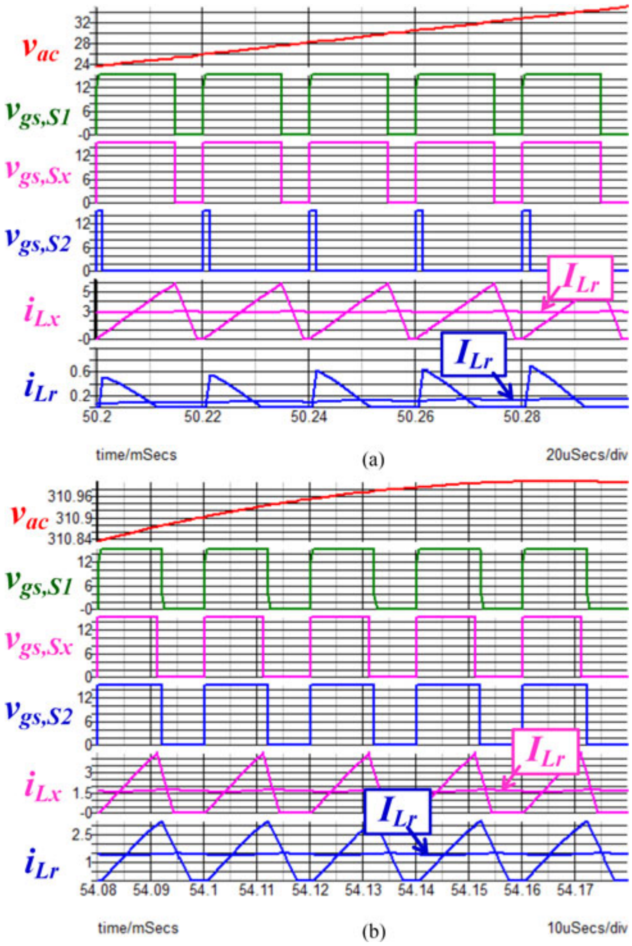

Fig. 19. Simulated line voltage, gating signals, and corresponding current waveforms of the propose PV micro-inverter for (a) Case I and (b) Case II.

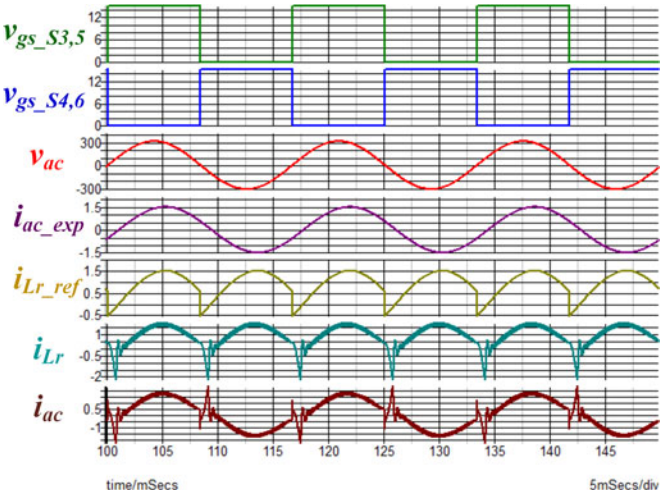

Fig. 20. Key simulated waveforms of the modified proposed circuit.

Theoretically, the proposed PV micro-inverter cannot provide reactive power because of its circuit structure. However, in Fig. 5, if a synchronous rectifier switch S_{LD} is adopted to replace the diode D_3 and the diode D_4 is removed, the proposed PV micro-inverter can provide reactive power. However, the amount of reactive power is limited and the output ac line current will be distorted with higher THD even if the inductance of L_r is increased for the CCM operation. The key simulated waveforms of the modified circuit are shown in Fig. 20. To provide reactive power, the inductor current reference i_{Lr_ref} should be modified to match the change of the conducting pair of the unfolder. Theoretically, an expected, the injected ac current $i_{\mathrm{ac\_exp}}$ will become sinusoidal with a phase lag to the grid voltage. However, the inductor current i_{Lr} cannot track i_{Lr_ref} very well during the sudden current change transient. Although the desired reactive power (power factor 0.95 lagging) can be achieved, the current THD will increase (up to 30%), too.

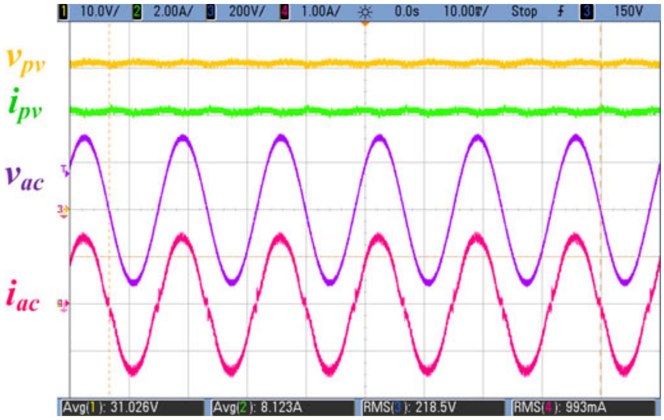

Fig. 21. Experimental waveforms for steady state operation with rated PV power.

Therefore, the proposed PV micro-inverter is not dedicated for reactive power delivering. However, the proposed PVCD strategy can be adopted by different circuit topologies that are capable of reactive power delivering. Besides, it is also possible that the proposed PVCD strategy can be applied to different applications, such as a PFC converter, to eliminate the need of the electrolytic capacitor.

For the prototype hardware circuit with the specifications shown in Table V, the microcontroller unit (MCU) dsPIC33FJ16GS502 is adopted to realize the proposed PVCD strategy. Similar to the simulation condition, the measured steady state operation waveforms with rated PV power are shown in Fig. 21, where from the top to the bottom are PV voltage $v_{\rm PV}$, PV current $i_{\rm PV}$, grid ac voltage $v_{\rm ac}$, and grid ac current $i_{\rm ac}$. The measured waveforms show that $v_{\rm PV}$ and $i_{\rm PV}$ have very small ripples ($\Delta v_{\rm PV} = 1.9$ V and $\Delta i_{\rm PV} = 0.5$ A) while the proposed PV micro-inverter produces a sinusoidal current $i_{\rm ac}$ in phase with the grid voltage $v_{\rm ac}$. It reveals that the proposed PV micro-inverter with PVCD strategy can achieve very good current decoupling requirement without using large electrolytic capacitors. It also should be mentioned that there is no abrupt disturbance in the input PV power or the output ac current because of the absence of mode-change control, which is utilized by the conventional SPPD strategy.

The measured gating signals for S_x and S_2 as well as the current waveforms for i_{Lx}, and i_{Lr} are shown in Fig. 22, where those ones for Case I operation are shown in Fig. 22(a) and those ones for Case II are shown in Fig. 22(b). Due to the channel limitation of the oscilloscope, only selected key waveforms are shown to verify the operation of the prototype hardware circuit.

By adopting the P&O method to fulfill the MPPT function, the maximum power of PV panel can be well traced as shown in Fig. 23. Waveforms shown in the upper portion of Fig. 23 are the measured power, voltage, and current of the PV panel as well as the ac grid voltage and injected ac line current where the partially magnified waveforms are shown in the lower portion of Fig. 23. These measured waveforms verify that the proposed PV micro-inverter can extract the maximum power from the PV panel automatically while injecting a sinusoidal ac current into the grid.

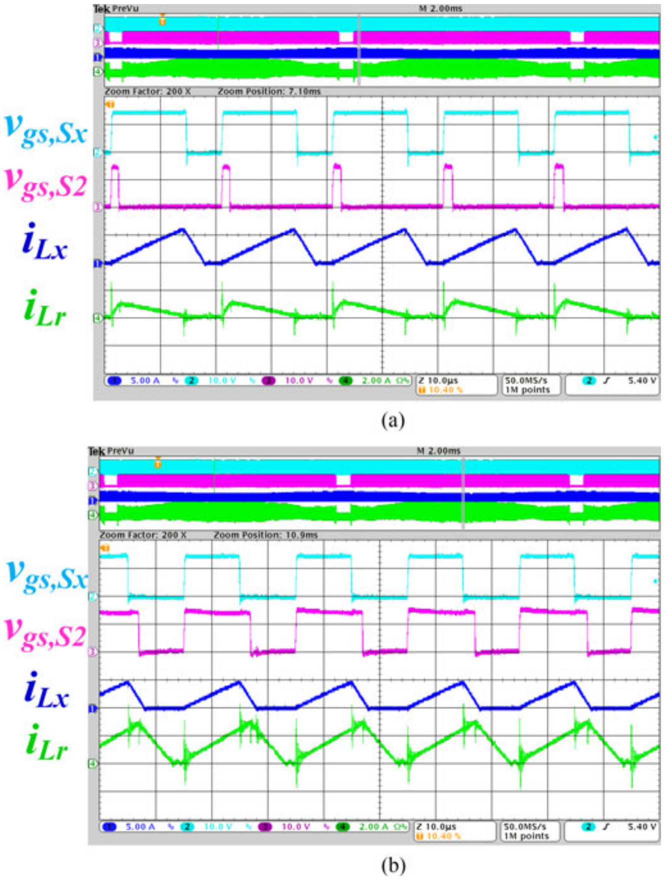

(a)

(b)

Fig. 22. Measured gating signal and current waveforms for different operation cases. (a) Case I. (b) Case II.

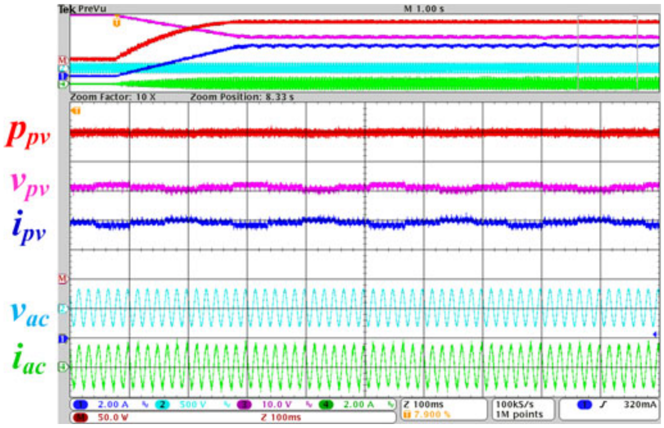

Fig. 23. Experimental results of the MPPT feature for the proposed PV micro-inverter.

Dynamic performance of the proposed PV micro-inverter with PVCD strategy is also tested. Fig. 24(a) and (b) shows the measured key waveforms of the input and output terminals of the prototype hardware circuit under different PV input power variation scenarios. Assuming a sudden solar illumination decreases, the output power of the PV panel will drop 100 W (42% of the rated power) abruptly and the measured waveforms are shown in Fig. 24(a). It can be seen that the MPPT feature for the

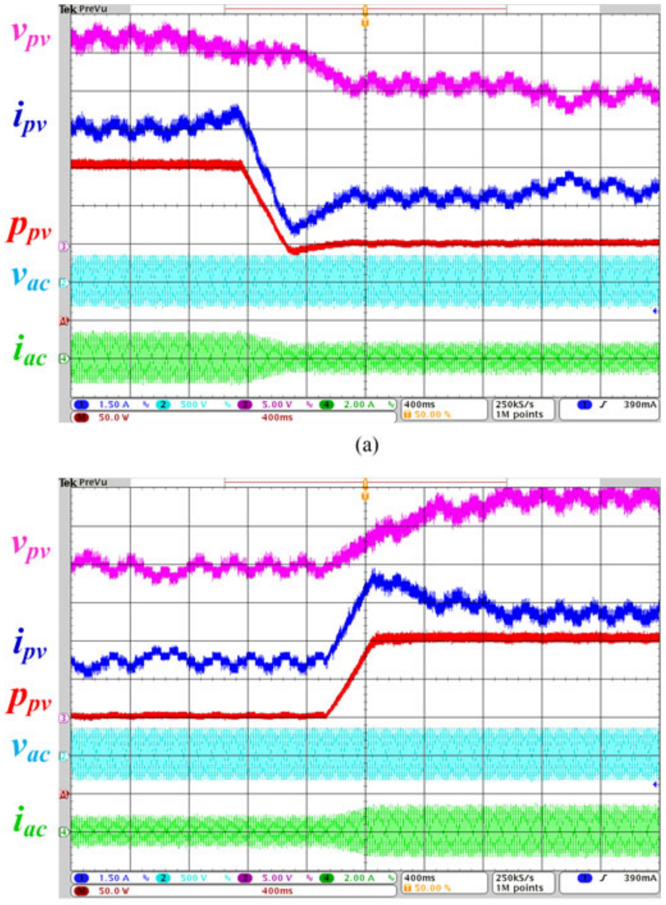

(a)

(b)

Fig. 24. Experimental results of the proposed PV micro-inverter with input PV power variations. (a) 100 W PV power decreasing. (b) 100 W PV power increasing.

PV panel can be quickly achieved after the solar illumination decreasing and a smooth transient of the output ac current drop can also be obtained. On the other hand, when the PV panel power increases suddenly, the proposed PV micro-inverter can achieve the similar good MPPT performance, as shown in Fig. 24(b).

One of the main goals of this paper is to eliminate the need of electrolytic capacitor. To quantify the reduction of decoupled capacitor C_x, a PV-side capacitor $C_{\mathrm{PV\_ss}}$ in the conventional single-stage PV micro-inverter is compared. Since the voltage ratings of C_x and $C_{\mathrm{PV\_ss}}$ are different, it is more reasonable to compare their charge storage capability, i.e., $Q = CV$. If the conventional single-stage flyback-type micro-inverter without any decoupling circuit is used for the PV system with the same voltage and power ratings, the required input capacitance for $C_{\mathrm{PV\_ss}}$ will be 10.6 mF to achieve a 2 V voltage ripple at the input PV panel. The required charge storage capability of capacitor C_x has 97% reduction compared to capacitor $C_{\mathrm{PV\_ss}}$, if a 25 μF capacitor with 500 V voltage rating and a 10.6 mF capacitor with 40 V voltage rating are selected for C_x and $C_{\mathrm{PV\_ss}}$, respectively.

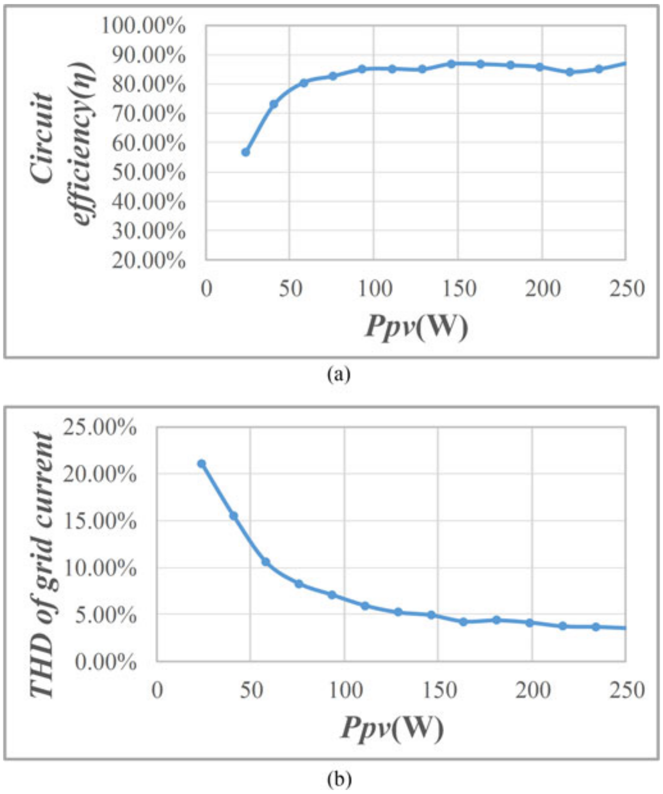

(a)

(b)

Fig. 25. Measured efficiency and THD of the prototype circuit. (a) Efficiency curve. (b) THD of grid current.

TABLE VI
POWER LOSS ANALYSIS OF THE PROTOTYPE CIRCUIT AT FULL LOAD

Components	Conduction Loss	Switching s	Leakage Loss	Reverse Recovery Loss	Core Loss
S_1	1.29 W	0.36 W	N/A	N/A	N/A
S_2	0.42 W	1.22 W	N/A	0.15 W	N/A
S_x	1.63 W	1.22 W	N/A	N/A	N/A
$S_3 - S_6$	0.24 W	0 W	N/A	N/A	N/A
D_1	1.41 W	N/A	N/A	1.23 W	N/A
D_2	0.73 W	N/A	N/A	0.57 W	N/A
D_3	0.71 W	N/A	N/A	0.57 W	N/A
D_4	0.88 W	N/A	N/A	0.57 W	N/A
L_{PV}	0.20 W	N/A	N/A	N/A	0.55 W
L_x	2.66 W	N/A	N/A	N/A	1.30 W
L_r	0.12 W	N/A	N/A	N/A	1.14 W
L_{ac}	0.12 W	N/A	N/A	N/A	1.14 W
T_1	2.06 W	N/A	7.10 W	N/A	2.07 W

The power conversion efficiency and the THD of grid current, measured by the power meter Yokogawa WT1800, are depicted as Fig. 25(a) and (b). Table VI shows the power loss analysis of the prototype circuit at full load. The output current THD is below 5% when the output power is higher than 50% load. Based on the operation modes and the derived equations in the previous sections, the power loss analysis of the prototype circuit at full load can be obtained. The total power loss at full load is consistent with the measurement result. Circuit efficiency of prototype hardware circuit so far is not good enough. The main reason for the dissatisfied circuit efficiency is many component counts of the proposed circuit. Moreover, no soft-switch techniques are used for any switches in the proposed circuit. Therefore, more conduction and switching losses are produced by these devices.

In addition to optimize the selection of the devices, reducing the number of components and including soft-switch techniques are the two ways for improving the circuit efficiency. On the other hand, Table VI can also be provided to electrical engineers for improving circuit efficiency if the proposed approach is considered to be developed. Although the efficiency performance is not satisfied and should be improved in the future, the experimental results of the prototype circuit do verify the performance of the proposed PV micro-inverter with PVCD strategy.

VI. CONCLUSION

A novel PV micro-inverter with the PVCD strategy is proposed in this paper. With the CDT inside, the proposed PV micro-inverter can draw constant current from the PV panel while delivering a sinusoidal current into the ac grid. Good MPPT performance can be obtained without using large electrolytic capacitors, so the reliability of the proposed PV micro-inverter can be greatly improved. In this paper, the operation principle and the component design of the proposed PV micro-inverter with PVCD strategy are presented. Different to the conventional power decoupling approach, the proposed PVCD control is based on the concept of current decoupling. Computer simulations and the experimental results are shown to verify the performance of the proposed PV micro-inverter with PVCD strategy. Although the prototype hardware circuit has unsatisfactory circuit efficiency and limited reactive power providing, the proposed circuit proves great ability of current decoupling function whenever steady state output or dynamic change of PV power.

REFERENCES

[1] Q. Li and P. Wolfs, "A review of the single phase photovoltaic module integrated converter topologies with three different DC link configurations, " *IEEE Trans. Power Electron.*, vol. 23, no. 3, pp. 1320–1333, May 2008.

[2] S. B. Kjaer, J. K. Pedersen, and F. Blaabjerg, "A review of single-phase grid-connected inverters for photovoltaic modules," *IEEE Trans. Ind. Appl.*, vol. 41, no. 5, pp. 1292–1306, Sep.–Oct. 2005.

[3] H. Hu, S. Harb, N. Kutkut, I. Batarseh, and Z. J. Shen, "A review of power decoupling techniques for micro-inverters with three different decoupling capacitor locations in PV Systems," *IEEE Trans. Power Electron.*, vol. 28, no. 6, pp. 2711–2726, Jun. 2013.

[4] H. Hu, X. Fang, F. Chen, Z. J. Shen, and I. Batarseh, "A modified high-efficiency LLC converter with two transformers for wide Input-Voltage range applications," *IEEE Trans. Power Electron.*, vol. 28, no. 4, pp. 1946–1960, Apr. 2013.

[5] A.C. Nanakos, G. C. Christidis, and E. C. Tatakis, "Weighted efficiency optimization of flyback micro-inverter under improved boundary conduction mode (i-BCM)," *IEEE Trans. Power Electron.*, vol. 30, no. 10, pp. 5548–5564, Oct. 2015.

[6] W.-J. Cha, Y.-W. Cho, J.-M. Kwon, and B.-H. Kwon, "Highly efficient micro-inverter with soft-switching step-up converter and single-switch-modulation inverter," *IEEE Trans. Ind. Electron.*, vol. 62, no. 6, pp. 3516–3523, Jun. 2015.

[7] A. Amirahmadi, L. Chen, U. Somani, H. Hu, N. Kutkut, and I. Bartarseh, "High efficiency dual-mode current modulation method for low-power DC/AC inverters," *IEEE Trans. Power Electron.*, vol. 29, no. 6, pp. 2638–2642, Jun. 2014.

[8] Z. Zhang, X.-F. He, and Y.-F. Liu, "An optimal control method for photovoltaic grid-tied-interleaved flyback micro-inverters to achieve high efficiency in wide load range," *IEEE Trans. Power Electron.*, vol. 28, no. 11, pp. 5074–5087, Nov. 2013.

[9] B. Chen *et al.*, "A high-efficiency MOSFET transformerless inverter for nonisolated micro-inverter applications," *IEEE Trans. Power Electron.*, vol. 30, no. 7, pp. 3610–3622, Jul. 2015.

[10] B. Tamyurek and B. Kirimer, "An interleaved high-power flyback inverter for photovoltaic applications," *IEEE Trans. Power Electron.*, vol. 30, no. 6, pp. 3228–3241, Jun. 2015.

[11] S. Jiang, D. Cao, Y. Li, and F. Z. Peng, "Grid-connected boost-half-bridge photovoltaic micro-inverter system using repetitive current control and maximum power point tracking," *IEEE Trans. Power Electron.*, vol. 27, no. 11, pp. 4711–4722, Nov. 2012.

[12] D. Meneses, O. Garcia, P. Alou, J. A. Oliver, and J. A. Cobos, "Grid-connected forward micro-inverter with primary-parallel secondary-series transformer," *IEEE Trans. Power Electron.*, vol. 30, no. 9, pp. 4819–4830, Sep. 2015.

[13] O. Gagrica, P. H. Nguyen, W. L. Kling, and T. Uhl, "Micro-Inverter curtailment strategy for increasing photovoltaic penetration in Low-Voltage networks," *IEEE Trans. Sustainable Energy*, vol. 6, no. 2, pp. 369–379, Apr. 2015.

[14] Y. Fang and X. Ma, "A novel PV micro-inverter with coupled inductors and double-boost topology," *IEEE Trans. Power Electron.*, vol. 25, no. 12, pp. 3139–3147, Dec. 2010.

[15] S.-M. Chen, T.-J. Liang, L.-S. Yang, and J.-F. Chen, "A safety enhanced, high step-up DC–DC converter for AC photovoltaic module application," *IEEE Trans. Power Electron.*, vol. 27, no. 4, pp. 1809–1817, Apr. 2012.

[16] S. Zengin, F. Deveci, and M. Boztepe, "Decoupling capacitor selection in DCM flyback PV micro-inverters considering harmonic distortion," *IEEE Trans. Power Electron.*, vol. 28, no. 2, pp. 816–825, Feb. 2013.

[17] T. Shimizu, K. Wada, and N. Nakamura, "Flyback-type single-phase utility interactive inverter with power pulsation decoupling on the DC input for an AC photovoltaic module system," *IEEE Trans. Power Electron.*, vol. 21, no. 5, pp. 1264–1272, Sep. 2006.

[18] S. B. Kjaer and F. Blaabjerg, "Design optimization of a single phase inverter for photovoltaic applications," in *Proc. IEEE Power Electron. Spec. Conf.*, 2003, pp. 1183–1190.

[19] I. Serban and C. Marinescu, "Active power decoupling circuit for a single-phase battery energy storage system dedicated to autonomous microgrids," in *Proc. IEEE Int. Symp. Ind. Electron.*, Jul. 4–7, 2010, pp. 2717–2722.

[20] K.-D. Kim, Y.-H. Kim, J.-G. Kim, Y.-C. Jung, and C.-Y. Won, "A new active power decoupling technique for three-port flyback inverter," in *Proc. Int. Power Electron. Motion Control Conf.*, Jun. 2–5, 2012, pp. 1159–1163.

[21] S. Harb, M. Mirjafari, and R. S. Balog, "Ripple-port module-integrated inverter for grid-connected PV applications," *IEEE Trans. Ind. Appl.*, vol. 49, no. 6, pp. 2692–2698, Nov.–Dec. 2013.

[22] Y.-M. Chen and C.-Y. Liao, "Three-port flyback-type single-phase micro-inverter with active power decoupling circuit," in *Proc. IEEE Energy Convers. Congr. Expo.*, Sep. 17–22, 2011, pp. 501–506.

[23] P. T. Krein and R. S. Balog, "Cost-effective hundred-year life for single-phase inverters and rectifiers in solar and LED lighting applications based on minimum capacitance requirements and a ripple power port," in *Proc. IEEE Appl. Power Electron. Conf. Expo.*, Feb. 15–19, 2009, pp. 620–625.

[24] D. Li, Z. Zhang, B. Xu, M. Chen, and Z. Qian, "A method of power decoupling for long life micro-inverter," in *Proc. IEEE Ind. Electron. Society*, Nov. 7–10, 2011, pp. 802–807.

[25] T. Hirao, T. Shimizu, M. Ishikawa, and K. Yasui, "A modified modulation control of a single-phase inverter with enhanced power decoupling for a photovoltaic ac module," in *Proc. Eur. Conf. Power Electron. Appl.*, 2005, pp. 1–10.

[26] S. Gao, W. Wu, N. He, and C. Chen, "A power decoupling circuit research based on interleaved parallel flyback micro-inverter," in *Proc. Int. Conf. Intell. Human-Mach. Syst. Cybern.*, Aug. 26–27, 2013, pp. 210–213.

[27] P. Neshaastegaran and H. R. Karshenas, "A power decoupling technique for single-stage micro-inverter in ac-module application," in *Proc. Drive Syst. Technol. Conf. Power Electron.*, Feb. 5–6, 2014, pp. 120–125.

[28] N. Pragallapati and V. Agarwal, "Single phase solar PV module integrated flyback based micro-inverter with novel active power decoupling," in *Proc. IET Int. Conf. Power Electron., Mach. Drives*, Apr. 8–10, 2014, pp. 1–6.

[29] H. Hu *et al.*, "A three-port flyback for PV micro-inverter applications with power pulsation decoupling capability," *IEEE Trans. Power Electron.*, vol. 27, no. 9, pp. 3953–3964, Sep. 2012.

[30] T. Shimizu and S. Suzuki, "Control of a high-efficiency PV inverter with power decoupling function," in *Proc. IEEE Int. Conf. Power Electron. ECCE Asia*, May 30–Jun. 3 2011, pp. 1533–1539.

[31] H. Hu, S. Harb, N. H. Kutkut, Z. J. Shen, and I. Batarseh, "A single-stage micro-inverter without using electrolytic capacitors," *IEEE Trans. Power Electron.*, vol. 28, no. 6, pp. 2677–2687, Jun. 2013.

[32] C.-Y. Liao, Y.-M. Chen, and W.-H. Lin, “Forward-type micro-inverter with power decoupling,” in *Proc. IEEE Appl. Power Electron. Conf. Expo.*, Mar. 17–21, 2013, pp. 2852–2857.

[33] H. Wang, H. S. H. Chung, and W. Liu, “Use of a series voltage compensator for reduction of the DC-link capacitance in a capacitor-supported system,” *IEEE Trans. Power Electron.*, vol. 29, no. 3, pp. 1163–1175, Mar. 2014.

[34] W. Liu, K. Wang, H. S. h. Chung, and S. T. H. Chuang, “Modeling and design of series voltage compensator for reduction of DC-link capacitance in grid-tie solar inverter,” *IEEE Trans. Power Electron.*, vol. 30, no. 5, pp. 2534–2548, May 2015.

[35] X. Lyu, N. Ren, Y. Li, and D. Cao, “A SiC-based high power density single-phase inverter with in-series and in-parallel power decoupling method,” *IEEE J. Emerg. Sel. Topics Power Electron.*, vol. 4, no. 3, pp. 893–901, Sep. 2016.

[36] S. Qin, Y. Lei, C. Barth, W. C. Liu, and R. C. N. Pilawa-Podgurski, “Architecture and control of a high energy density buffer for power pulsation decoupling in Grid-Interfaced applications,” in *Proc. IEEE 16th Workshop Control Model. Power Electron.*, Vancouver, BC, Canada, 2015, pp. 1–8.

[37] B. J. Pierquet and D. J. Perreault, “A Single-Phase photovoltaic inverter topology with a Series-Connected energy buffer,” *IEEE Trans. Power Electron.*, vol. 28, no. 10, pp. 4603–4611, Oct. 2013.

Chien-Yao Liao (S’11) received the B.S. degree in electrical engineering from the National Taiwan University of Science and Technology, Taipei, Taiwan, in 2010, and the M.S. degree in electrical engineering in 2011 from National Taiwan University, Taipei, where he is currently working toward the Ph.D. degree.

His current research interests include PV micro-inverter and battery charger for renewable energy application.

Wen-Shiun Lin was born in Chiayi, Taiwan, in 1989. He received the B.S. degree in electrical engineering from National Sun Yat-Sen University, Kaohsiung, Taiwan, in 2011, and the M.S. degree in electrical engineering from National Taiwan University, Taipei, Taiwan, in 2013.

He is currently with the National Taiwan University. His current research interests include small-signal modeling and control in large power system.

Yaow-Ming Chen (S’96–M’98–SM’05) received the B.S. degree from National Cheng-Kung University, Tainan, Taiwan, and the M.S. and Ph.D. degrees from the University of Missouri, Columbia, MO, USA, in 1989, 1993, and 1997, respectively, all in electrical engineering.

From 1997 to 2000, he was with I-Shou University, Taiwan, as an Assistant Professor. From 2000 to 2008, he was with National Chung Cheng University, Taiwan. In 2008, he joined National Taiwan University, where he is currently a Professor in the Department of Electrical Engineering. His current research interests include power electronic converters and renewable energy.

Cheng-Yen Chou (S’91–M’97) received the B.S. degree from National Tsing-Hua University, Hsinchu, Taiwan, and the M.S. degree from the National Yunlin University of Science and Technology, Yunlin, Taiwan, in 1997. He is currently working toward the Ph.D. degree at the National Taiwan University of Science and Technology, Taipei, Taiwan.

He is also with Darfon Electronic Corp., Taoyuan.